A micromechanical based finite element model approach to accurately predict the effective thermal properties of micro-aerated chocolate

D. Bikos [a],[*], G. Samaras [a], M.N. Charalambides [a], P. Cann [a], M. Masen [a], C. Hartmann [b], J. Vieira [c], A. Sergis [a], Y. Hardalupas [a]

[a] Department of Mechanical Engineering, Imperial College London, United Kingdom
[b] Nestlé Research Centre, Lausanne, Switzerland
[c] Nestlé Product Technology Centre, York, United Kingdom

ARTICLE INFO

ABSTRACT

Micro-aeration is a method to modify the sensorial attributes of chocolate but also affects the material properties of chocolate, which in turn, determine its material response during manufacturing and oral processes. This study aims to define the effect of micro-aeration on the thermal properties of chocolate by considering the changes of chocolate microstructure due to micro-aeration. Micro-aeration was found to alter the chocolate microstructure creating a layer of a third phase at the porous interfaces, which is argued to consist of cocoa butter of higher melting properties. A multiscale Finite Element Model is developed, which was confirmed by macroscale heat transfer measurements, to parametrically simulate the structural changes of micro-porous chocolates at the microscale level and estimate their effective properties, such as thermal conductivity and specific heat capacity. The developed multiscale computational model simulates the porous chocolate as a two-phase (chocolate- pores) or three-phase material (chocolate-cocoa butter layer- pores). The investigation identified a new, complex transient thermal mechanism that controls the behaviour of micro-aerated chocolate during melting and solidification. The results showed a maximum 13% reduction of k_{eff} and 15% increase of C_{peff} with 15% micro-aeration resulting to a slower transient heat transfer through the micro-aerated chocolate. The reason is that the micro-aerated chocolate can store a larger amount of thermal energy than its solid counterpart. This effect slows down the transient heat transfer rate in the chocolate and modifies melting/solidification rate and impacts sensorial attributes during oral processing and cooling during manufacturing.

1. Introduction

Micro-aeration has been widely practised in the food industry to create new and improved consumer experiences whilst, at the same time, being able to reduce the content of sugars and fats without adversely affecting key sensorial attributes, i.e. sweetness (Bikos et al., 2021a; Haedelt, Beckett, & Niranjan, 2007; Minor, Vingerhoeds, Zoet, de Wijk, & van Aken, 2009). In addition, micro-aeration is reported to lead to the design of new chocolate products with tuned and sophisticated sensorial profiles (Bikos et al., 2021a; Campbell & Mougeot, 1999; Haedelt et al., 2007; Rovers, Sala, van der Linden, & Meinders, 2016). Even though it is reported that micro-aeration significantly affects sensory perception, the mechanisms responsible for this change are not yet fully understood.

Chocolate structure from an engineering perspective can be considered as a composite material consisting of a variety of hard particles, the sugar crystals, cocoa solids, and in some cases milk powder, dispersed in a continuous fat matrix of cocoa butter and in some cases milk fat (Chen & Mackley, 2006; Glicerina, Balestra, Dalla Rosa, & Romani, 2016; Rousseau & Smith, 2008). The volume fraction of the hard particles in typical chocolate ranges from 50 to 60 *wt*% that are dispersed within a continuous fat matrix. There is vast literature on chocolate, linking the effect of structure and compositional variations to its material properties (Afoakwa, Paterson, Fowler, & Vieira, 2009; Do, Hargreaves, Wolf, Hort, & Mitchell, 2007; Glicerina et al., 2016; Reinke et al., 2016). These properties are key parameters to control manufacturing and oral processes (le Reverend, Fryer, & Bakalis, 2008; Skamniotis, Edwards, Bakalis, Frost, & Charalambides, 2020; Skamniotis, Elliott, & Charalambides, 2017). Micro-aeration, even at small porosity levels, has been reported to significantly affect material

---

* Corresponding author.
  E-mail address: d.bikos17@imperial.ac.uk (D. Bikos).

properties, such Young's modulus, thermal conductivity, and friction coefficient (Bikos et al., 2021a; Bikos et al., 2021b; Bikos et al., 2022; Samaras, 2021; Samaras et al., 2020) which consequently affect its structural breakdown during oral processing under mechanical, thermal, and frictional loads.

Several techniques have been employed to study the effect of porosity on the thermal properties of a material, including experimental, analytical, and computational (Cao, Yu, & Qin, 2012; Cernuschi, Ahmaniemi, Vuoristo, & Mäntylä, 2004; Huang, 1971; Jackson & Leach, 1993; Singh, Tanaka, & Endo, 2007; Smith et al., 2013; Zhang, Fang, Li, & Tao, 2017). In foods, mainly experimental and analytical methods have been employed to predict the effect of porosity on overall thermal properties (Carson, Lovatt, Tanner, & Cleland, 2006; Carson, Wang, North, & Cleland, 2016; Hamdami, Monteau, & le Bail, 2003; Shah, Tong, & Lund, 2000). Our recent study proposed a multiscale computational model to evaluate the effect of micro-aeration in chocolate considering the structural changes at a microscale level (Bikos et al., 2022). This research highlighted unexpected trends of heat transfer behaviour of micro-porous chocolate under transient heat transfer conditions. More specifically, a consistent rise of specific heat capacity was depicted which is uncommon for porous materials. These conditions are important and relevant to oral processing, but not limited to that. For example, cooling during manufacturing controls the quality of the final product and depends on the chocolate's unsteady heat transfer behaviour. The origins of the displayed complex transient thermal behaviour of micro-aerated chocolate are thought to stem from a novel mechanism of microstructural modification of the specific heat capacity of chocolate with porosity that cause amplification effects which are not described by general uniform macroscopic models. Our initial interpretation is that these amplification effects originate from the presence of a third phase located between the chocolate matrix and the gas pores (Bikos et al., 2021b). This argument is also supported by recent literature on aerated edible fats reporting that the third phase is cocoa butter (Binks & Marinopoulos, 2017; Mishima, Suzuki, Sato, & Ueno, 2016) of different crystallisation form. In this work, the effect of the pore-chocolate interface on material properties is hence investigated.

However, apart from the additional thermal (different thermal properties) and geometrical effects (thickness of the third phase layer) added by the presence of a third phase, also the quality of the thermal contact at the interface of the third phase and the matrix, affect the overall heat transfer behaviour of the material. Mainly in engineering materials, several publications have reported techniques to investigate the effect of heat propagation at the interface of an inclusion or a pore (le Quang, He, & Bonnet, 2011; Lee, Lee, Ryu, & Ryu, 2018; Nan, Birringer, Clarke, & Gleiter, 1997). These thermal resistance mechanisms are referred across the literature as interfacial resistance and often is associated with the Kapitza number (le Quang et al., 2011), which associates specific thermal resistance effects at the micro or nanoscale. This interfacial resistance arises because of the molecular thermal interactions between vastly different material states (e.g. solid-liquid, solid-gas, gas-liquid) and the incompatibility in the way heat propagates through such interfaces. In the case of aerated chocolate, Kapitza resistance effects are expected to exist at the interface between the third phase and the matrix (solid) of the material. The kapitza resistance depends on the thermal conductivity and the thickness of the interface (Lee et al., 2018; Marcos-Gómez, Ching-Lloyd, Elizalde, Clegg, & Molina-Aldareguia, 2010). Since these parameters are often difficult to measure, parametric studies are often employed to quantify the thermal resistance mechanisms at the interface indirectly by analytical or computational methods (Lee et al., 2018; Marcos-Gómez et al., 2010). However, according to the authors' best knowledge no available literature has studied and modelled the interfacial thermal resistance of multiphase composites in conjunction with simultaneous thermal storage effects due to phase change in foods. Both effects are expected to change the thermal response of such systems, which can alter the perceived oral processing experience.

The aim of this study is, hence, to incorporate these heat transfer mechanisms in the modelling process of chocolate materials with varying levels of porosity and quantify their contribution to sensorial attributes. More specifically, the multiscale computational model of this research assumes a novel heat energy storage mechanism at the pore's interface by considering chocolate as a complex three-phase system at the microscale consisting of chocolate, cocoa butter pore's interface layer and a gaseous pore. An interfacial thermal resistance mechanism between the three modelled phases is explored to provide new understanding of the complex heat transfer phenomena reported in micro-aerated chocolate. The developed multiscale model (Bikos et al., 2022) is extended to include the presence of a third phase and the computational results are compared to transient heat transfer measurements from a bespoke test rig and Differential Scanning Calorimetry (DSC) measurements. This comparison evaluates the ability of the new computational multiscale model to link changes in the chocolate microstructure during aeration, as evidenced by recorded X-ray tomography images, with changes in the chocolate's thermal properties.

2. Materials and methods

This section presents a brief summary of the materials and methodology used for the experimental and computational procedures with all necessary details to reproduce the presented investigations. Additional details regarding the manufacturing process of the material of the samples (cocoa butter and chocolate), heat transfer testing rig, and multiscale computational models is available in (Bikos, 2022; Bikos et al., 2022).

2.1. Materials

Chocolate samples with porosity levels of 0%, 10%, and 15% were provided by the Nestlé Product Technology Centre (NPTC) (York, UK) and used for the chocolate thermal experiments with a novel, bespoke, heat transfer test rig; an overview of the rig is provided in section 2.2. All chocolate samples exhibited a typical composition of 44 *wt%* sugar particles, 27*wt%* cocoa fat, 10 *wt%* whole milk powder, 6 *wt%* non-fat cocoa solids and 0.3 *wt%* sunflower lecithin. Refined, un-tempered cocoa butter was also provided by NPTC and tested using the heat transfer rig. The cocoa butter specimens were subsequently subjected to a conventional tempering process, i.e., using a double bath and the seeding method, followed by cooling in rectangular moulds with dimensions: $110 \times 25 \times 15$ *mm³* (Bikos et al., *2022*).

The initial geometry of the chocolate was provided by NPTC in the form of a rectangular beam with dimensions: $80 \times 15 \times 8$ *mm³*. The chocolate geometries were further modified using a razor saw to final dimensions: $50 \times 8 \times 8$ *mm³*. The cocoa butter specimens were also modified in order to have the same dimensions as the chocolate samples to ensure consistency during thermal testing. The aspect ratio 1:1 of the cross section of the chocolate samples was selected to ensure uniform temperature distribution across the height of the sample, based on preliminary testing results.

The melting properties, such as the latent heat, specific heat capacity, and the temperature ranges where phase change occurs, for all types

Table 1

: Melting parameters of all types of chocolate (0%, 10%, and 15%) and cocoa butter (CB) samples obtained from the DSC experiments at 1 °**C** *min*⁻¹ (Bikos et al., 2022).

Sample	T_{onset} °C	T_{peak} °C	T_{end} °C	ΔH kJkg⁻¹	C_{psolid} kJkg⁻¹K⁻¹	$C_{pliquid}$ kJkg⁻¹K⁻¹
0%				15	2.6 ± 0.1	2.0 ± 0.3
10%	28	31	34	14	2.7 ± 0.2	2.1 ± 0.1
15%				14	2.8 ± 0.3	2.3 ± 0.1
CB		32		74	6.0 ± 1.0	4.9 ± 0.6

of chocolate and cocoa butter are summarised in Table 1. These values are quoted from the literature as measured from DSC experiments at a heating rate of 1 °C min^{-1} (Bikos et al., 2022).

2.2. Heat transfer experiments - methods

The developed heat transfer rig precisely thermoregulated the two ends of the beam-shaped samples described in section 2.1 independently and recorded spatial and temporal temperature profiles of their cores (half the specimens height $H/2$) at three different locations T_1, T_2, and T_3 using k-type thermocouples. These locations corresponded to distances of 16, 25 and 37.5 *mm* from the one end of the samples, as shown in Fig. 1.

In the setup of Fig. 1, the tested sample is supported by the aluminium blocks (used to ensure sample uniformity and thermal stability), which in turn, are heated or cooled independently from each side by the respective heating elements. Note that the experimental boundary conditions were fixed throughout the duration of the experiments, i. e., no temporal variation of the boundary conditions was performed during testing. All components of the test rig were thermally insulated using 3D-printed sleeves to provide better control of the generated heat fluxes. Four different testing scenarios were employed with boundary conditions summarised in Table 2. Scenarios 1 and 2 represent relatively moderate and rapid heating respectively from both sides of the heat transfer rig. The target temperature in these scenarios was selected so that the chocolate enters the phase transition range at different rates. Scenario 3 represents a cooling case with a target temperature outside the phase transition range. Scenario 4 represents a more complex testing scenario, i.e. heating one end and cooling on the other, to assess the predictive power of the computational model. Lower temperatures than 16 °C were not selected due to constraints of the testing rig to reach and maintain effectively temperatures lower than 7 °C from the ambient temperature (23 °C). The ambient/environmental temperature and relative humidity were fixed to 23°C and 50% respectively. The cocoa butter specimens were only subjected to scenario 3 because preliminary experiments in heating mode showed that the test sample geometry for the cocoa butter during heating was not preserved, unlike chocolate, since the cocoa butter melted and flowed out of the insulation sleeves.

The measurements from the heat transfer test rig of Fig. 1 are used to validate the multiscale computational model and the possible presence of a third phase at the chocolate interface. The temperature measurements from the cocoa butter specimens were used to estimate the thermal conductivity of cocoa butter, an important parameter for the computational models, as explained in the subsequent sections.
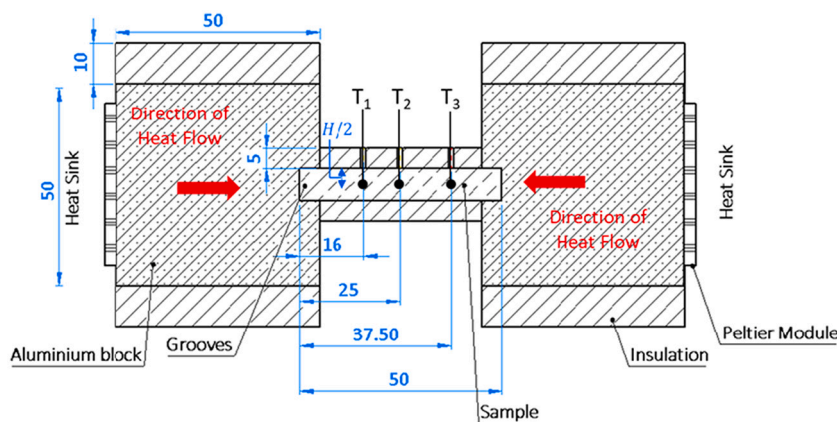
Table 2
Boundary conditions applied to each side of the samples on the heat transfer test rig from the Peltier modules for all testing scenarios.

Testing scenario	T_{left} [°C]	T_{right} [°C]
1	35	35
2	45	45
3	16	16
4	45	16

2.3. Development of finite element model at micro and macroscale

2.3.1. Micromechanical finite element model (micro-FEM)

A 3D Finite Element model at microscale (micro-FEM) was developed using Abaqus implicit solver (Simulia, 2017) with pores dispersed in the chocolate matrix to simulate the micro-aerated chocolate samples. The average pore size found in the tested micro-aerated chocolate is reported to be approximately 40 *μm* (Bikos et al., 2021b). The virtual geometry and coordinates of the pores were randomly generated using Macropac (Macropac, Oxford Materials, UK) and dispersed within a cubic domain. The size of this cubic domain was controlled in order to achieve the desired level of micro-aeration (10%, 12%, and 15%). Thus, the sizes of the RVEs for the 10%, 12%, and 15% chocolate were 0.32 *mm*, 0.3 *mm*, and 0.28*mm* respectively. Whilst the 12% chocolate was not tested experimentally, it was employed in the micromechanical FEM to add one more data point and assist the identification of the trends of the effect of porosity on the thermal properties of chocolate. The pore coordinates were utilised to create 3D spheres of 40 *μm* diameter, which represented the dispersed pores in the chocolate. The effect of poly-dispersed micro-pores on the thermal properties of chocolate was not studied in this work.

Macropac was also used to reproduce the cocoa butter shell geometry according to available X-ray tomography images in the literature (Bikos et al., 2021b), see Fig. 2a. The geometries of the 3D spheres and the duplicated scaled ones together with the cubic domain were imported on Abaqus (Simulia, 2017). A cut geometry tool available on Abaqus was utilised to subtract the geometries of the scaled 3D spheres from the initial sphere geometry to create the shell geometries of Fig. 2b and c. The size of the spherical shells was controlled to be the same as the whiter regions around the pores on the X-ray tomography image of Fig. 2a and the same for all micro-aerated chocolates.

As aforementioned, chocolate is a multiphase system consisting of microscopic features such as sugar, cocoa, and milk particles. Since the main focus of this work is to quantify the effect of micro-aeration on the thermal properties of chocolate, the solid chocolate was assumed to be a continuum single phase material with effective thermal properties as
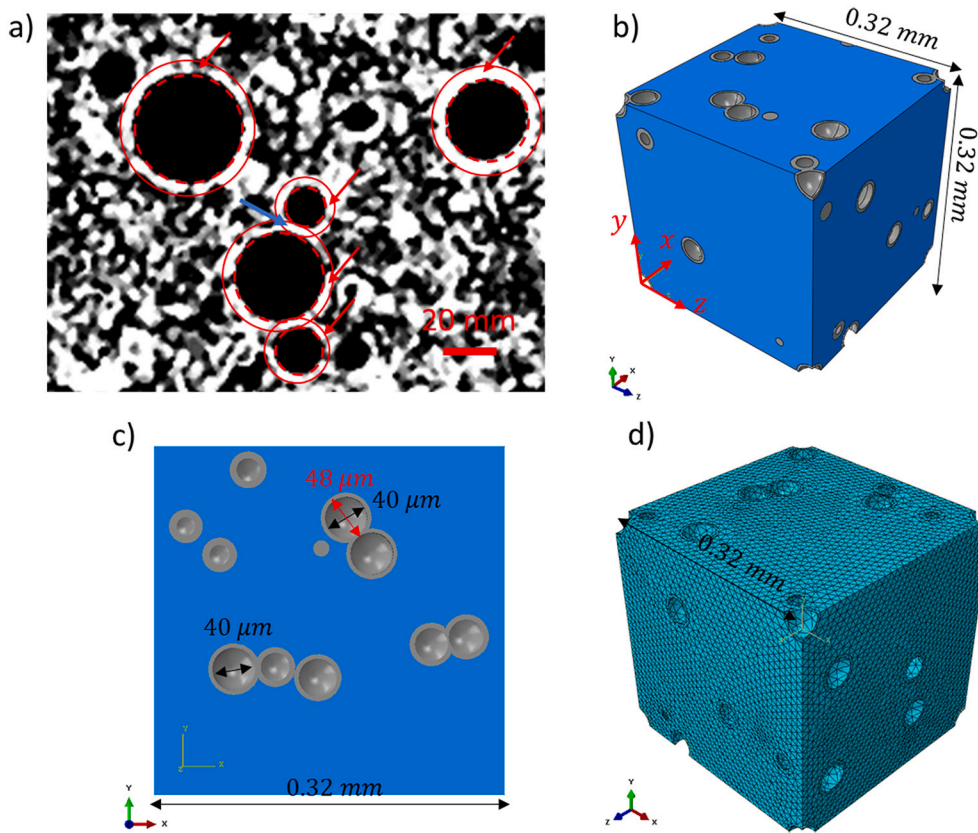

Fig. 1. Schematic side view representation of the heat transfer test rig configuration. The direction of the heat flow depicted with red arrows on the schematic represents a scenario where both ends of the sample are being heated. (For interpretation of the references to colour in this figure legend, the reader is referred to the web version of this article.)

Fig. 2. (a) X-ray tomography image for the 15% micro-aerated chocolate from Bikos et al. (Bikos et al., 2021b) showing the dispersed pores in the chocolate matrix and concentrated areas at the pore's interface. (b) Geometry domain with 100 spherical shells dispersed randomly inside the chocolate matrix in the case of 10% micro-aerated chocolate. (c) Section of the modelled microstructure domain for the 10% micro-aerated chocolate showing the dimensions of the pore and the third phase interfacial layer in the form of a shell. (d) Final meshed geometry of the 10% micro-aerated chocolate. The thickness of the shells was selected according to the thickness of the whiter regions around the pores on the X-ray tomography image (see red arrows in image a) and was constant for micro-aerated chocolates. (For interpretation of the references to colour in this figure legend, the reader is referred to the web version of this article.)

measured by the heat transfer rig and DSC experiments.

A chocolate matrix microstructure cubic domain with 100 randomly dispersed shelled pores was modelled. The assembled model containing the cocoa butter shell (grey colour) and the chocolate matrix (blue colour) can be seen in Fig. 2b. A dimensionalised section of the assembled model is shown in Fig. 2c. Interaction of two or more shells was also modelled since this was observed in the X-ray tomography images of the real chocolate microstructure (see blue arrow in Fig. 2a).

The volume of elements or commonly known as representative volume element (RVE) of Fig. 2b was meshed with a maximum of 720,000 linear 4-node heat transfer elements, as shown in Fig. 2d. The number of elements was varied depending on the RVE of different levels of porosity in order to accurately represent the microstructure geometry with the best possible mesh quality. The unit cell of Fig. 2d represents the RVE for the case of the 10% micro-aerated chocolate containing a total number of 320,000 elements. Mesh sensitivity analysis showed that any grid with 300,000 elements or higher led to converged results.

In Abaqus, the thermal resistance at the interface is employed in the form of thermal conductance (i.e. the inverse of thermal resistance, R), as shown in Eq. (1) (le Quang et al., 2011). Since the geometry dependent thermal resistance mechanisms at this interface are unknown, a parametric study was conducted to investigate the influence of interfacial thermal conductance, C, on the computed thermal properties, such as the bulk thermal conductivity and specific heat capacity.

$$C = \frac{1}{R} = \frac{k_{in}}{t_{in}} \tag{1}$$

where k_{in} is the thermal conductivity of the interface and t_{in} is the thickness of the interface.

The material properties, such as the thermal conductivity, specific heat capacity, latent heat, and density, of the non-aerated chocolate and cocoa butter are required for the micro-FEM calculations and are summarised in Table 3. The thermal conductivity of cocoa butter was

Table 3

: Material properties of chocolate and cocoa butter used in the Finite Element Models, macro-FEM and micro-FEM (Bikos et al., 2022).

Material Properties	Value	Units
Density of chocolate, $\rho_{0\%}$	1300	Kg/m^3
Specific heat capacity of solid chocolate, C_{P_s}	2600	J/Kg K
Thermal conductivity of solid chocolate, k_s	0.45	W/m K
Specific heat capacity of liquid chocolate, C_{p_l}	2000	J/Kg K
Thermal conductivity of liquid chocolate, k_l	0.55	W/m K
Latent heat of chocolate (0%), ΔH	15,000	J/Kg
Melting temperature (0%), T_m	304	K
Density of cocoa butter, ρ_{CB}	900	Kg/m^3
Specific heat capacity of solid cocoa butter, $C_{p_{CB,\,s}}$	6000	J/Kg K
Specific heat capacity of liquid cocoa butter, $C_{p_{CB,\,l}}$	4500	J/Kg K
Thermal conductivity of cocoa butter, k_{CB}	0.35	W/m K

calibrated using a macro-FEM model, based on the measurements from the heat transfer test rig. In Table 3, the thermal properties of the chocolate and cocoa butter specimens depend on the state, i.e. liquid (temperature higher than 34 °C, see Table 1) or solid (temperature lower than 28 °C, see Table 1).

To assess the micro-FEM predictions from the two-phase and the three-phase model approaches, the same RVE (see Fig. 2b) was employed for the two-phase system concept assuming that the third phase (shell material) indicated the same thermal and physical properties as the chocolate matrix. The two geometries were fully bonded (no interfacial resistance or high interfacial conductance) for the two-phase approach, whilst for the three-phase system approach the possibility of interfacial resistance in the form of gap interfacial thermal conductance was investigated. To investigate the effect of the interfacial resistance on the thermal properties of porous chocolate, using the micro-FEM simulation, C was varied from a relatively high arbitrary value, i.e. 10^5 W/m^{2}K, to a relatively small arbitrary value of 10^{-3} W/m^{2}K. The thermal

properties for the chocolate matrix (non-aerated chocolate) and spherical shells (cocoa butter) are summarised in Table 3.

As opposed to the specific heat capacity of cocoa butter, which was shown to depend on the state of the material (solid or liquid), the thermal conductivity of cocoa butter was assumed to be independent because this property was only calibrated using scenario 3 (cooling) when the material was at solid state. However, this does not affect the accuracy of the results, since the micro-FEM predictions presented in the following sections are normalised by the respective property of the chocolate matrix (k_{eff}/k_m). In addition, no differences between solid and liquid states were observed in these normalised values for other materials, i.e., all types of chocolates.

The effective thermal properties, estimated by the micro-FEM, were fed into the macro-FEM simulating the different testing scenarios in Table 2. In addition, the effective thermal properties were computed, considering the porous chocolate as a two-phase and three-phase system, and were compared to the specific heat capacity data as a function of porosity, as quoted in (Bikos et al., 2022). It is important to note that the latent heat, ΔH, of chocolate was found to be independent of porosity.

For the steady state heat transfer analysis, the only input parameter required for the Finite Element Models (FEM) is the thermal conductivity. On the other hand, the unsteady heat transfer models required material properties such as density, specific heat capacity, thermal conductivity, and latent heat.

To estimate the macroscopic effective thermal conductivity of the porous chocolate, k_{eff}, a steady-state heat transfer step was employed for the micro-FEM. This analysis was performed on the RVE of Fig. 2 for both the two-phase and three-phase systems and all porosity levels. The boundary conditions for the steady-state step were selected to be an arbitrary temperature difference ΔT at the bottom and top surface of 10 °C. It is important to highlight that the value of ΔT does not influence the resultant effective thermal conductivity of chocolate. The side surfaces were considered thermally insulated (see Fig. 3) according to the following formula:

$$\frac{\partial T}{\partial x_1}(0,t), \frac{\partial T}{\partial x_1}(0.32,t), \frac{\partial T}{\partial x_3}(0,t), \frac{\partial T}{\partial x_3}(0.32,t) = 0 \tag{2}$$

Under these boundary conditions, the effective thermal conductivity can be computed as follows:

$$k_{eff} = \frac{\dot{Q}_{|y=0}}{A\,\Delta T} t \tag{3}$$

where, $\dot{Q}_{|y=0}$ is the overall heat transfer rate at the bottom surface (y = 0) of the RVE, see Fig. 2b, t is RVE's thickness, which, for the example of Fig. 2b, is 0.32 mm, and A is the cross sectional area of the RVE.

To compute the macroscopic effective specific heat capacity of the porous chocolate, C_{peff}, an unsteady heat transfer step was employed.

The boundary conditions used for this analysis were a pulse of heat applied to the top surface of the RVE ($Q_{|y=0.32} = 0.5\ mJ$), see Fig. 2b. All other surfaces were considered thermally insulated (see Fig. 3) using the following set of equations:

$$\frac{\partial T}{\partial x_1}(0,t), \frac{\partial T}{\partial x_1}(0.32,t), \frac{\partial T}{\partial x_3}(0,t), \frac{\partial T}{\partial x_3}(0.32,t), \frac{\partial T}{\partial x_2}(0,t) = 0 \tag{4}$$

The pulse of heat was applied for a specified period of 1 s. After this period elapsed, the top surface was also considered to be insulated. The effective specific heat capacity for a single-phase material is described by:

$$C_{p_{eff}} = \frac{Q_{|y=0}}{\rho_{eff}\, V \Delta T} \tag{5}$$

where ρ_{eff} is the macroscopic effective mass density of the porous material, which is defined by the rule of mixtures, and V the volume of the RVE.

The unsteady heat transfer step is simulated until a specified rate of temperature change is reached, which indicates that a steady-state condition is achieved. This rate of temperature change was set to an arbitrary relatively small number of 10^{-5} °C/s.

For the three-phase system, the interfacial thermal resistance needs to be employed into the micro-FEM models in the form of gap conductance, C. The formula describing this effect follows Fourier's law as shown below (Lee et al., 2018):

$$q_{int} = C\Delta T \tag{6}$$

where q_{int} is the heat flux at the interface, and ΔT is the temperature difference at the interface due to the effect of the interfacial thermal resistance.

Thermal diffusivity is an important parameter to study the heat transfer behaviour of a solid and provides details regarding the temperature sensitivity and temporal and spatial response of a material to applied heat fluxes. This parameter quantifies the thermal energy that is conducted relative to the thermal energy that is stored in the material. The macroscopic thermal diffusivity, a_{eff}, is described by the following relationship:

$$a_{eff} = \frac{conduction}{stored\ thermal\ energy} = \frac{k_{eff}}{\rho_{eff}\, C_{p_{eff}}} \tag{7}$$

In the case of the micro-aerated chocolates with porosities of 10%, 12%, and 15%, all parameters of Eq. (4) are substituted by the respective effective properties, i.e. k_{eff}, C_{peff} and ρ_{eff}.

Even though thermal diffusivity is commonly employed to describe the heat transfer behaviour of solids, it is argued that it can be used for chocolate at a liquid state. This is because at temperatures up to 45 °C, chocolate behaves as a very viscous liquid, and hence, the dominant mode of heat transfer is assumed to be conduction without any motion
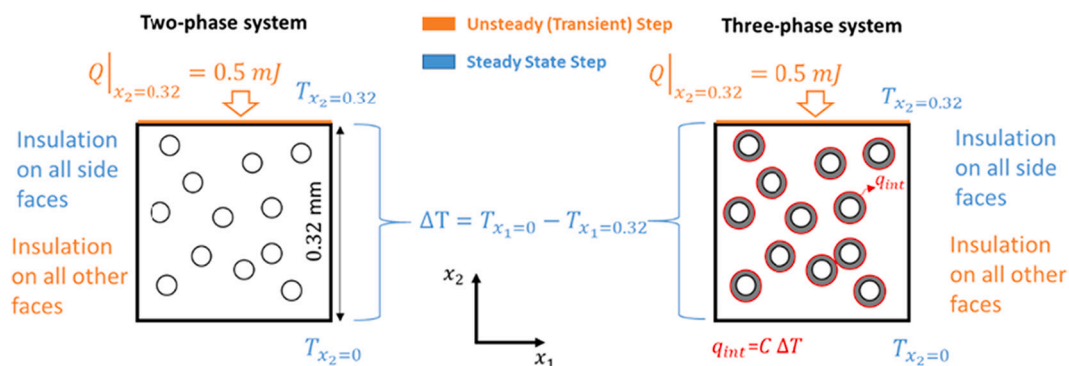

Fig. 3. Boundary conditions (BCs) for the 10% chocolate as a two-phase system (left) and three-phase system (right) under steady-state (BCs with blue colour) and unsteady (BCs with orange colour) conditions. The height of the RVE of this schematic, 0.32 mm, was selected to correspond to the desired porosity of 10%.

within the material. However, the traditionally derived thermal diffusivity attribute cannot be used to describe the transition of materials from solid to liquid phases and Eq. (7) cannot be used during that stage.

A modified thermal diffusivity is derived by the current study to reflect the diffusion of heat and therefore the thermal response of the material during this phase change. The derivation assumes that the phase change occurs at a given melting temperature. In reality, during phase change a temperature potential still is required to drive energy into/out of a material; the assumption of a singular temperature during phase change has been commonly made not only to characterise such materials but also to simplify similar relevant relationships in the field. As such, the derived phase change thermal diffusivity, a_{pceff}, of Eq. (8) relates the diffusion of heat through conduction and the stored thermal energy as latent heat capacity of the material (similar to the classic derivation of thermal diffusivity) during phase change:

$$a_{pc\,eff} = \frac{conduction}{stored\ thermal\ energy} = \frac{k_{eff}}{\rho_{eff}\,\Delta H}\,T_{peak} \quad (8)$$

where ΔH is the latent heat and T_{peak} is the melting temperature of the material corresponding to the peak point in a typical DSC curve, see Table 1.

To produce consistent units between Eqs. (7) and (8) and create a link between heat transfer events when chocolate changes phase or not, a characteristic temperature term was added in Eq. (5). This characteristic temperature was selected to be the melting temperature, T_m, of chocolate, which, for the 0%, 10% and 15% aerated chocolate, is constant at 304 K, see Table 3.

In the case of chocolate, Eq. (7) is only applicable for temperature thresholds outside the phase change range, which is between 28°C and 34°C see Table 1. In the case where phase change occurs, Eq. (8) should be employed.

2.3.2. Macromechanical finite element model (macro-FEM)

A 3D model with the same geometry and dimensions as the materials tested at the heat transfer rig was developed, see Fig. 4. Preliminary macro-FEM results showed that a mesh with 6200 8-node linear heat transfer elements delivers converged results which lie within the experimental error (1%) of the heat transfer rig. The highlighted volume with red edges in Fig. 4 corresponds to the volume in contact with the aluminium block (see Fig. 1), whilst the volume with blue colour edges in contact with the insulation material (see Fig. 1). The boundary
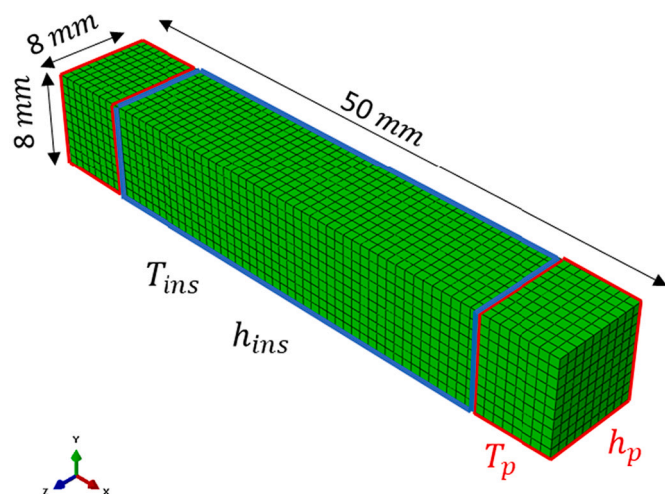

Fig. 4. Geometry of the macro-FEM model simulating the experimental conditions of the thermal rig. The highlighted regions with red colour denote areas that are in contact with the aluminium blocks and associated with the set temperature controlled by the Peltier modules, whilst the regions with blue colour depict areas that are in contact with the insulated sleeves.

conditions used for the macro-FEM modelling for all thermal loading scenarios are summarised in Table 4. The heat transfer coefficients required at the boundaries of the tested samples are denoted as h_p and h_{ins} for the boundary associated with the volume in contact with the aluminium block (see volume highlighted with red in Fig. 4) and the boundary in contact with the insulated sleeves (see volume highlighted with blue in Fig. 4) respectively. These values were calibrated by the macro-FEM model (Bikos et al., 2022), and found to be independent of the tested material. The set temperature values at the boundaries are denoted with the same notation as the associated heat transfer coefficients, T_p and T_{ins}, see Table 4.

The material properties, such as thermal conductivity, specific heat capacity, latent heat and density, which were required for the macro-FEM model in the case of the non-aerated chocolate are summarised in Table 3. In the case of the micro-aerated chocolates, the thermal conductivity and specific heat capacity were measured from the micro-FEM at steady and unsteady states respectively as described in the previous section. The value of the thermal conductivity of cocoa butter was calibrated to produce the best possible fit to the measurements for scenario 3. An arbitrarily selected starting value of 0.1 W/mK for the thermal conductivity both at solid and liquid state was selected, which was within the range of commonly reported values in the literature (0.09 W/mK – 0.12 W/mK) (Debaste, Kegelaers, Liégeois, Ben Amor, & Halloin, 2008; Maleky & Marangoni, 2011).

The thermal conductivity of cocoa butter was then adjusted using the macro-FEM model to match the experimental data. This analysis was employed on cocoa butter to reversely calculate the thermal conductivity of cocoa butter using the macro-FEM model and the temporal evolution of the temperature measurements from the heat transfer testing rig.

The macro-FEM predictions for the 10% and 15% micro-aerated samples using the two-phase, the three-phase without interfacial thermal resistance, and three-phase with interfacial resistance ($C = 0.01\ W/m^2K$) systems were compared to the temporal evolution of the temperature measurements from the heat transfer testing rig.

3. Finite element model results and discussion

3.1.1. Computation of thermal conductivity of cocoa butter, k_{CB}

In this section the thermal conductivity of cocoa butter is computed, which is required for the three-phase micro-FEM model, followed by micro-FEM and macro-FEM simulations.

The outcome of scenario 3 for the case of cocoa butter measurements from the heat transfer test rig is summarised in Fig. 5. The thermal conductivity of cocoa butter was 'calibrated' using the macro-FEM to create the best possible fit between experiments and model predictions, resulting to a value of 0.35. The value of the thermal conductivity of cocoa butter was adjusted to fit the temporal temperature data of all thermocouples, as shown in Fig. 5. A satisfactory value was reached when the smallest possible uncertainty amongst the model predictions

Table 4

: Boundary conditions used for the macro-FEM under different loading scenarios. Each column indicates the heat transfer coefficient h together with the associated temperature values. The temperature values T_p and T_{ins} are equal to experimental values of Table 2.

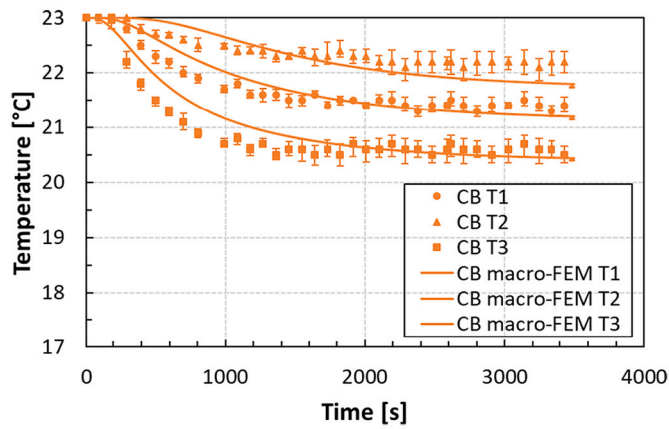| Testing scenario	h_p [W/m^2K]	T_p [°C]	h_{ins} [W/m^2K]	T_{ins} [°C]
1	70	35	4	23
2		45	4	
3		16	8	
4		45 (left) 16 (Right)	4	

Fig. 5. Temporal temperature evolution predicted from the macro-FEM compared to the heat transfer experiments for cocoa butter. The term "*CB*" in the legend refers to the cocoa butter measurements, T_1, T_2, and T_3, see Fig. 1.

and all experimental temperature-time curves was observed. The minimisation of the uncertainty between model predictions and experiments was also confirmed by the least square method (average R^2 : 0.95). This value represents the thermal conductivity of cocoa butter at the solid state and is found to be 22% lower than the respective value for the non-aerated chocolate at solid state, see Table 3, which is aligned with reports from the literature (Debaste et al., 2008). Slightly higher differences are observed at location T_3 than the other two locations of the thermocouples. This effect could potentially be explained by the fact that cocoa butter is assumed to consist of one crystallisation form. In addition, the thermal properties, such as specific heat capacity and latent heat, of cocoa butter and chocolate are reported to be dependent on the rate of the applied heat transfer, and this dependence is not included in the presented models. Depending on the location of the thermocouple, different rates of heat transfer are expected to be experienced in the cocoa butter. However, even with these simplifications, a reasonable agreement between experiments and computations with a maximum difference (T_3 location) less than 3% is indicated. This gives additional confidence regarding the computation of the thermal properties of cocoa butter, such as specific heat capacity $C_{p_{CB}}$ and thermal conductivity k_{CB}.

The lower value of thermal conductivity of cocoa butter, along with the increased value of specific heat capacity (see Table 1) as opposed to the respective properties of chocolate, suggests an overall lower rate of heat transfer in the case of cocoa butter. Assuming that cocoa butter is concentrated around the pore's interface, which exhibits higher storage

capability (140% higher C_p & 390% higher ΔH) and a lower rate of heat transfer (22% lower k) than the solid chocolate, means that the average heat transfer response of the micro-aerated chocolate will be affected. More specifically, the average values of specific heat capacity and thermal conductivity are expected to increase and decrease respectively, leading to slower heat transfer response inside the material.

3.1.2. Micromechanical finite element model (micro-FEM) results

The steady-state micro-FEM computations using the two-phase and three-phase systems on an RVE, such as the one of Fig. 2b, are summarised in Fig. 6a for porosity levels 10%, 12%, 15%. The normalised effective thermal conductivity, k_{eff}, relative to the thermal conductivity of the chocolate matrix, k_m, is plotted against porosity for three chocolate systems: (i) two-phase, (ii) three-phase with fully bonded thermal contact (very high interfacial thermal conductance $C = 10^7$), and (iii) three-phase with thermal resistance mechanism at the interface of chocolate-cocoa butter (different values of C). A decrease of k_{eff}, for a given porosity level, is suggested by the micro-FEM for the three-phase system compared to the two-phase system. The difference between k_{eff} under the same porosity level for different values of C is increasing with increasing porosity. This is aligned with reports in the literature on various composite materials (Lee et al., 2018; Marcos-Gómez et al., 2010).

Moreover, the micro-FEM computations showed a significant effect of interfacial thermal conductance on the k_{eff} value where a maximum of 13% reduction in k_{eff} is reported for 15% micro-aerated chocolate when the fully bonded thermal contact is changed to a thermal contact with relatively low thermal conductance ($C = 0.001\ W/m^2K$). The dependence of the normalised k_{eff}/k_m data on C is presented in Fig. 6b. For all types of chocolate, an s-shaped curve is observed where k_{eff}/k_m is relatively constant both at relatively low and relatively high values of conductance. The reason lies in the fact that a finite amount of energy can be stored/dissipated at an interface with given dimensions. An increase is depicted in the $k_{eff}/k_m - C$ curve at the transition from low values of thermal conductance, $C = 0.1\ W/m^2K$, to higher values of thermal conductance, $C = 10\ W/m^2K$. After that, the ratio k_{eff}/k_m converges to a constant value.

The dependence of $\frac{k_{eff}}{k_m}$ on C is also greatly influenced by the size of the pores (Marcos-Gómez et al., 2010). However, this dependence exceeds the scope of this work. Based on studies on composite materials with imperfect interfaces, the size of the pore shifts the overall s-shaped $k_{eff}/k_m - C$ curve along the horizontal direction (Marcos-Gómez et al., 2010). This is explained by the fact that thermal conductance is influenced by the surface area of the interface, and hence, is expected to decrease with increasing pore size, suggesting that smaller sized
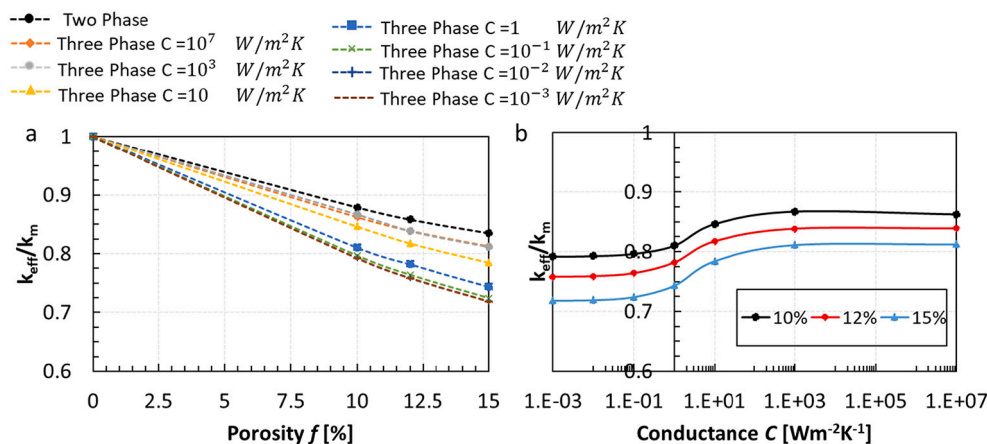

Fig. 6. (a) Results from the micro-FEM model using a third phase at the pore-chocolate interface showing the dependence of k_{eff}/k_m on the thermal conductance C of the interface as a function of porosity; (b) k_{eff}/k_m data as a function of thermal conductance C.

interfaces are greatly affected by the behaviour of the interface.

The unsteady (transient) micro-FEM computations using the two-phase and three-phase systems are summarised in Fig. 7a for chocolates with different levels of porosity. The normalised specific heat capacity is plotted against porosity for different values of C. Based on the results of Fig. 7a, an increasing trend of C_{peff} against porosity is suggested when the three-phase microstructure is introduced, as opposed to the two-phase system (see dotted black line), where C_{peff} is slightly affected by porosity, i.e. less than 4% increase with 15% micro-aeration. Moreover, based on the micro-FEM parametric study for different values of C, the C_{peff} data are not greatly influenced by the thermal conductance at the chocolate matrix-cocoa butter shell interface. This can be seen in Fig. 7b where the C_{peff}/C_{pm} is plotted against C for porosity levels 10%, 12%, and 15%.

A good agreement is observed between the C_{peff} micro-FEM predictions and DSC measurements for 10% and 15% micro-aerated chocolate, see Table 1, and shown in Fig. 7. Specifically, the three-phase micro-FEM predictions follows relatively accurately (less than 4% from the average value) the increasing trend of C_{peff} with porosity, which is true for both chocolate types and both chocolate states, i.e. solid (blue scatter in Fig. 7a) and liquid (red scatter in Fig. 7a). For the first time, the micro-FEM prediction for the three-phase system for micro-aerated chocolates captures the increasing trend of C_{peff} with micro-aeration level, providing additional confidence to the argument posed regarding the presence of a third phase at the pore-chocolate interface believed to be cocoa butter.

To assess the difference in the heat transfer response amongst the three types of chocolate, in terms of material's ability to store thermal energy, the thermal diffusivity is plotted in Fig. 8 against porosity. The normalised thermal diffusivity is computed considering both the two-phase and three-phase systems for the three types of chocolate, exploring the possibility of an interfacial resistance mechanism. It is important to highlight that the results of Fig. 8a refer to a state when no phase change occurs in the chocolate, whilst the data of Fig. 8b when chocolate changes phase.

The results of Fig. 8a show a drastic difference between the two-phase and the three-phase systems with a maximum difference of 11% for porosity level of 15%. This difference increases even further when thermal resistance is included at the chocolate matrix-cocoa butter interface with a maximum of 20% for porosity of 15% and thermal conductance lower than 0.1. This means that the micro-aerated chocolate can store higher amounts of thermal energy, which will be released into the chocolate system with a delay, affecting oral processing as well as manufacturing processes. The inclusion of a third phase increases even further the ability of chocolate to store thermal energy due to the higher specific heat capacity and thermal conductivity of cocoa butter relative to those of chocolate. The presence of an interfacial thermal resistance mechanism at the pore-cocoa butter interface increases further the decreasing trends of a_{eff}/a_m with porosity.

On the other hand, the transient heat transfer response of the chocolate as a function of porosity, when phase change occurs, is illustrated in Fig. 8b. Fig. 8b is constructed using Eq. (5) and is only valid when phase change occurs in the chocolate. Similar to Fig. 8a, the ability of the material to store thermal energy decreases with increasing porosity and decreases even further considering the chocolate as a three-phase system with an additional interfacial thermal resistance mechanism at the cocoa butter-pore's interface. Comparing the two graphs of Fig. 8, a smaller difference in the heat transfer response amongst all types of chocolate is observed when the phase change occurs. The reason is that latent heat and melting temperature were found to be independent of porosity, see Table 3. Hence, the only different parameters in Eq. (5) amongst all types of chocolate are the thermal conductivity and the density.

3.1.3. Macromechanical finite element model (macro-FEM) results

The macroscale behaviour of the chocolate is considered next. The temperature predictions from the macro-FEM model at locations T_1, T_2, and T_3 for 10% micro-aerated chocolate is shown in Fig. 9 together with the respective measurements (see scatters in Fig. 9) for all four scenarios. In Fig. 9, all types of solid lines represent the macro-FEM predictions using the different approaches described in the previous section.

Based on the macro-FEM results of Fig. 9, there is a minor difference (maximum 1.6%) between the macro-FEM predictions using thermal properties computed assuming a two-phase and a three-phase system for the microstructure. In addition, the macro-FEM computation, assuming thermal resistance (corresponding to $C = 10^{-2}$ W/m^2K) at the chocolate-cocoa butter interface, leads to more accurate predictions (maximum 3.4%, see T_2 in Fig. 9b), based on the experimental results, compared to the already very good (maximum 5%, see T_2 in Fig. 9b) predictions by the macro-FEM that assumes a two-phase system for the micro-aerated chocolate. Especially, in all cases except for temperature predictions at T_2 for scenario 2 (see Fig. 9b), the steady-state temperature predictions match the experimental results.

On the other hand, in Fig. 10, there is noticeable deviation amongst the macro-FEM results for the 15% micro-aerated chocolate from the different approaches, i.e. two-phase system, three-phase system, three-phase system with low thermal conductance. This deviation amongst the different approaches is more pronounced for 15% micro-aerated chocolate due to the higher difference of k_{eff}/k_m at the 15% porosity
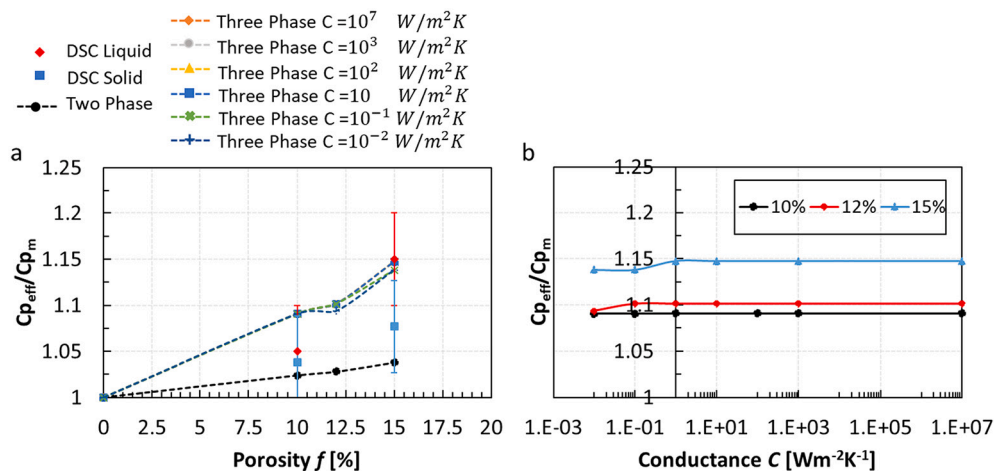

Fig. 7. (a) Computations from the micro-FEM using a third phase at the pore-chocolate interface showing the dependence of C_{peff}/C_{pm} on thermal conductance C as a function of porosity; (b) C_{peff}/C_{pm} as a function of thermal conductance C. The scatter plots in image a represent the DSC measurements, see Table 1, whilst the dotted lines the computations for chocolate with porosities 10%, 12%, and 15%. The lines are employed to distinguish measurements and predictions.
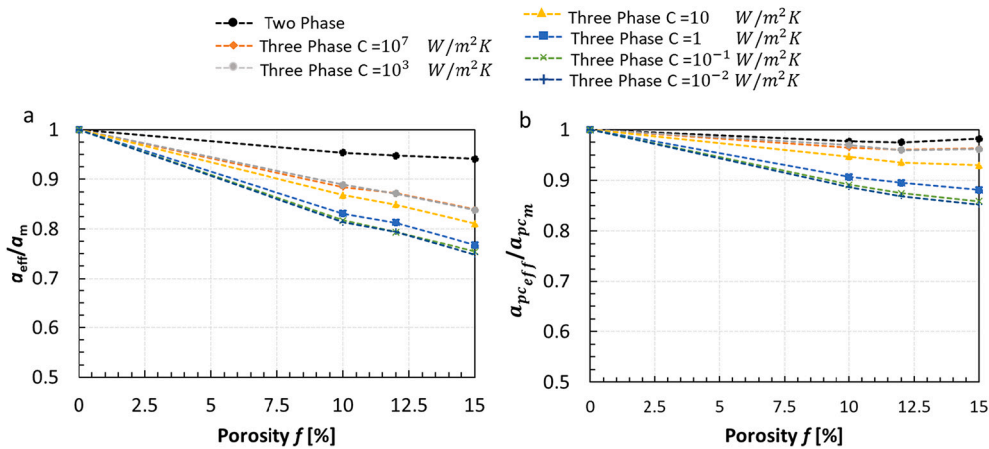
Fig. 8. (a) Normalised a_{eff}/a_m for different chocolate systems, i.e. two-phase and three-phase with interfacial thermal conductance, as a function of porosity. The data refer to solid chocolate – i.e. no phase change. (b) Normalised a_{pceff}/a_{pcm} data for the same chocolate systems as (a) but at the chocolate melting temperature.
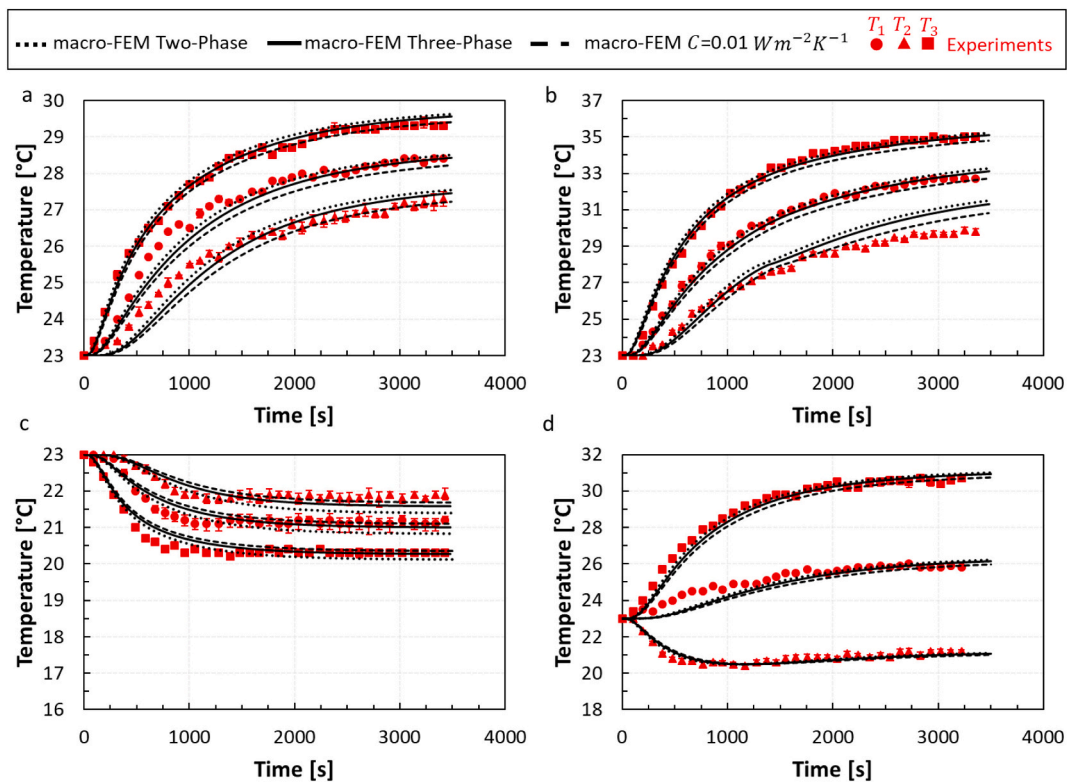

Fig. 9. Temporal evolution of temperature at different positions along the chocolate samples for 10% micro-aerated chocolate, predicted from the macro-FEM using the thermal properties from the micro-FEM, compared to the measurements (scatter) from the thermal rig. The three different solid lines represent the macro-FEM predictions using thermal properties from the micro-FEM assuming a two-phase microstructure (dotted line), three-phase microstructure (solid line), three-phase microstructure and relatively low interfacial thermal conductance (dashed line). The graphs show macro-FEM predictions for (a) scenario 1, (b) scenario 2, (c) scenario 3 and (d) scenario 4.

(see Fig. 10a). The macro-FEM based on the effective thermal properties from the three-phase micro-FEM predicts the temperature better (maximum difference 5%, see T_2 in Fig. 10b) when compared to the measurements. Especially the macro-FEM model, assuming $C = 10^{-2}$ W/m^2K at the chocolate-cocoa butter interface, leads to an almost perfect match (maximum difference 2.4%, see T_2 in Fig. 10b) to the experimental results, see Fig. 10. This is true for all four scenarios.

Therefore, the multiscale (micro-FEM and macro-FEM) computational investigation provided further proof regarding the presence of a third phase, cocoa butter, at the pore-chocolate interface. The multiscale numerical model considering the presence of a third phase was able to

capture accurately the increasing trend of specific heat capacity with increasing porosity as evident by the DSC measurements and at the same time produced more accurate predictions, especially for the 15% micro-aerated chocolate, of the experimental results from the heat transfer test rig. This is the first time that a multiscale Finite Element Model is able to capture the increased trends of specific heat capacity of chocolate with porosity accurately.

To assess the predictive power of the three model approaches (two-phase, three-phase and three-phase with interfacial thermal resistance), the percentage differences between the macro-FEM predictions and the thermocouple measurements for the case of 15% micro-aerated
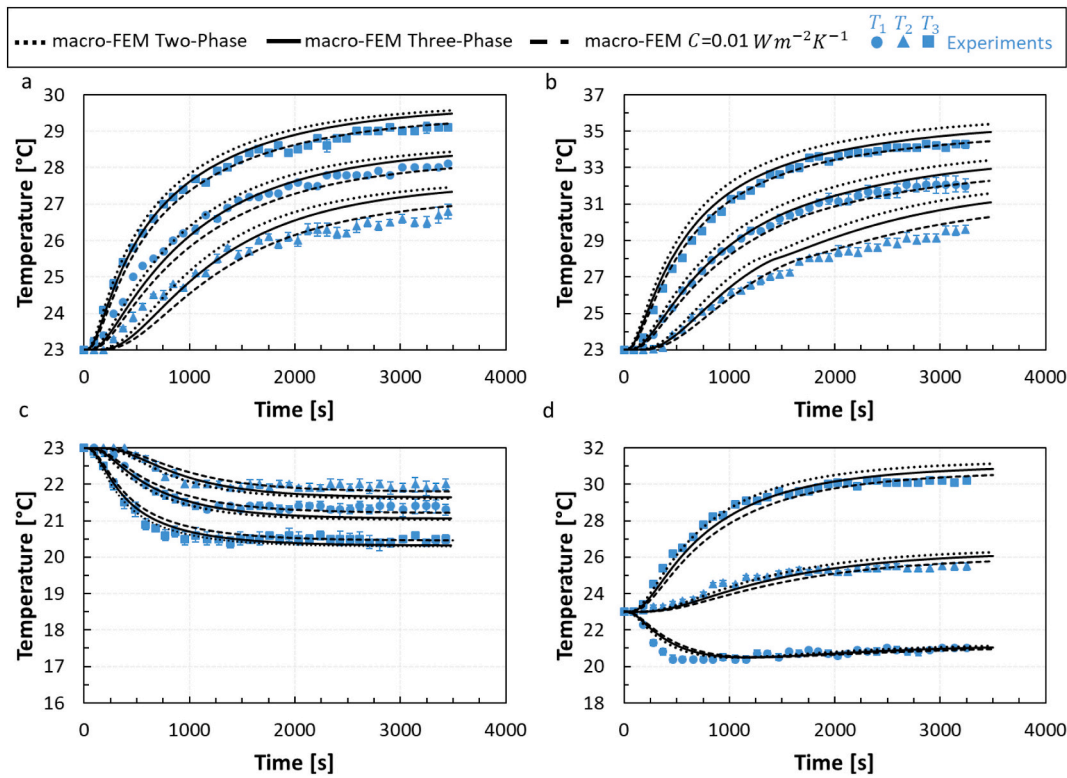
Fig. 10. Temporal evolution of temperature for 15% micro-aerated chocolate, predicted from the macro-FEM using the thermal properties from the micro-FEM, compared to the measurements (scatter). The three different solid lines represent the macro-FEM predictions using thermal properties from the micro-FEM assuming a two-phase microstructure (dotted line), three-phase microstructure (solid line), three-phase microstructure and relatively low interfacial thermal conductance (dashed line). The graphs show macro-FEM predictions for (a) scenario 1, (b) scenario 2, (c) scenario 3 and (d) scenario 4.

chocolate and scenario 4 are summarised in Fig. 11. As shown in Fig. 11, the three-phase assumption with or without interfacial thermal resistance reduces the differences at all thermocouple locations at steady-state conditions. Almost perfect fit is found between model predictions and thermocouple measurements when steady-state condition is reached, and interfacial thermal resistance is assumed. Slightly higher errors are observed, for all cases, at early stages of the experiment and at

the T_2 location. This might be explained by the fact that the thermal properties of chocolate were assumed to be independent of the heat transfer rate. At the three locations (T_1, T_2, and T_3), heat transfer rates are expected to vary. Similar differences were observed for all testing scenarios and types of chocolate.

Based on the close fit between the model predictions with low thermal conductance at the chocolate-cocoa butter shell interface and
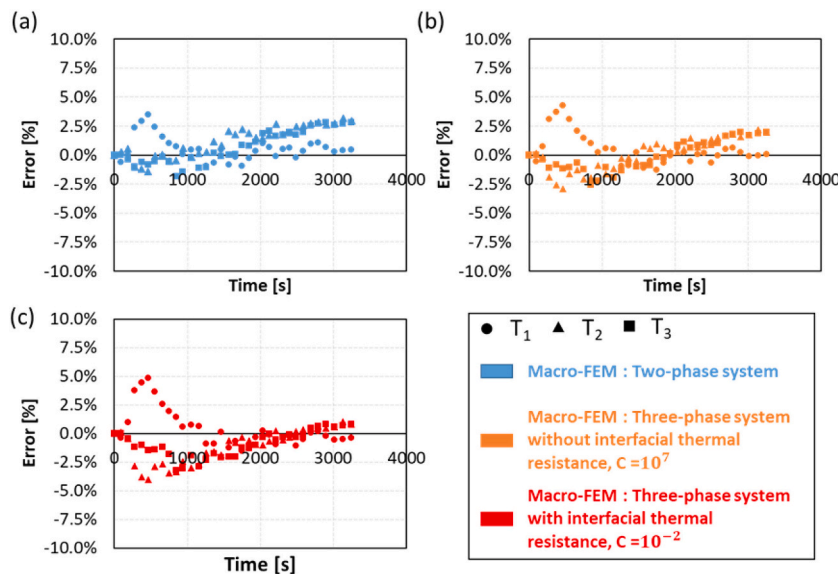

Fig. 11. Percentage difference between the macro-FEM predictions and the experimental measurements in locations T_1, T_2, and T_3 of the chocolate specimen. More specifically, the percentage difference between the macro-FEM (a) two-phase model, (b) three-phase without interfacial thermal resistance, and (c) three-phase model with interfacial thermal resistance of 10^{-2} and the experiments is presented. The legend of the three graphs is shown in the lower right corner of the figure.

the measurements, it is believed that an additional thermal resistance mechanism is present at the interface of the chocolate matrix and the cocoa butter shell. The outcome supported the assumption of an interfacial thermal resistance mechanism for porous chocolate. However, the causes of this mechanism remain unknown and require further investigation.

The effect of cocoa butter that is concentrated at the pores' interface and the effect of the interfacial thermal resistance on the rate of heat transfer at two characteristic locations within the RVE for the case of 15% chocolate is visualised in Fig. 12. These locations correspond to a point close to the cocoa-butter shell in the chocolate matrix (black point) and a point inside the cocoa butter cell (red point), as shown in Fig. 12a. The rate of heat transfer is plotted in Fig. 12b for these two locations for cases where chocolate is assumed as a two-phase material, a three-phase material without interfacial thermal resistance (high thermal conductance of 10^7 was chosen to model this scenario) and a three-phase material with a relatively high interfacial thermal resistance (low thermal conductance of 10^{-2}). The latter model was more accurate compared to the other micro-FEM approaches (see Fig. 9 and Fig. 10). In the same figure, the temperature difference (image c) and heat fluxes in the y-direction (image d) are plotted for chocolate without and relatively high interfacial thermal resistance. The selected time steps of the contour plots are just before the peak of the applied heat (time = 0.47 s) and after the removal of heat (time = 1.07 s). These results are obtained using the unsteady (transient) micro-FEM, which simulates a calorimetric type test where a controlled amount of heat is applied to an insulated RVE until a steady-state condition is reached, as described in section 2.3.1.

The results of Fig. 12b highlight a maximum difference of 8% in the heat transfer rate between the two-phase and the three-phase micro-FEM model without interfacial thermal resistance. However, when

interfacial thermal resistance is assumed, the heat transfer rate inside the cocoa butter shell is approximately 50% lower (see time = 0.57 s in Fig. 12b) than the other two cases (two-phase and three-phase with high C), see Fig. 12. Moreover, a delay in the peak heat transfer rate is observed when a low thermal conductance of 10^{-2} is assumed.

For a more representative comparison, the temperature difference and the heat fluxes in the y-direction due to the presence of heat are plotted for two cases ($C=10^7$ and $C=10^{-2}$) in Fig. 12 for two time increments. Based on the contour plots of Fig. 12c, cocoa butter exhibits lower temperatures (except for the top surface where heat is applied) than the regions surrounding it when a relatively high interfacial thermal resistance is assumed. This observation is also supported by Fig. 12d, which shows that only a small amount of heat flux can penetrate the third phase due to the presence of interfacial thermal resistance between the chocolate matrix and the cocoa butter. Moreover, for the case with $C=10^{-2}$, the trapped heat inside the cocoa butter is released into the system with a delay as shown in Fig. 12c and Fig. 12d (see time = 1.07 s). However, at locations away from the pores and the third phase, heat fluxes and the temperature differences of similar magnitudes are observed between these two cases with $C=10^7$ and $C=10^{-2}$.

Potentially, a form of incompatibility, e.g., chemical, between the chocolate matrix and the third phase interfaces occurs. This is because the cocoa butter concentrated at the pore interface might indicate a different crystallisation form from the cocoa butter that is dispersed in the rest of the material. This argument is confirmed by studies on aerated cocoa butter, which has shown that the concentrated cocoa butter at the surface of a pore exhibited a different melting point compared to the cocoa butter dispersed in the rest of the material, crystal forms VI vs V. These types of crystals exhibit higher melting points as opposed to the crystals present in chocolate, i.e. V-type. Consequently,
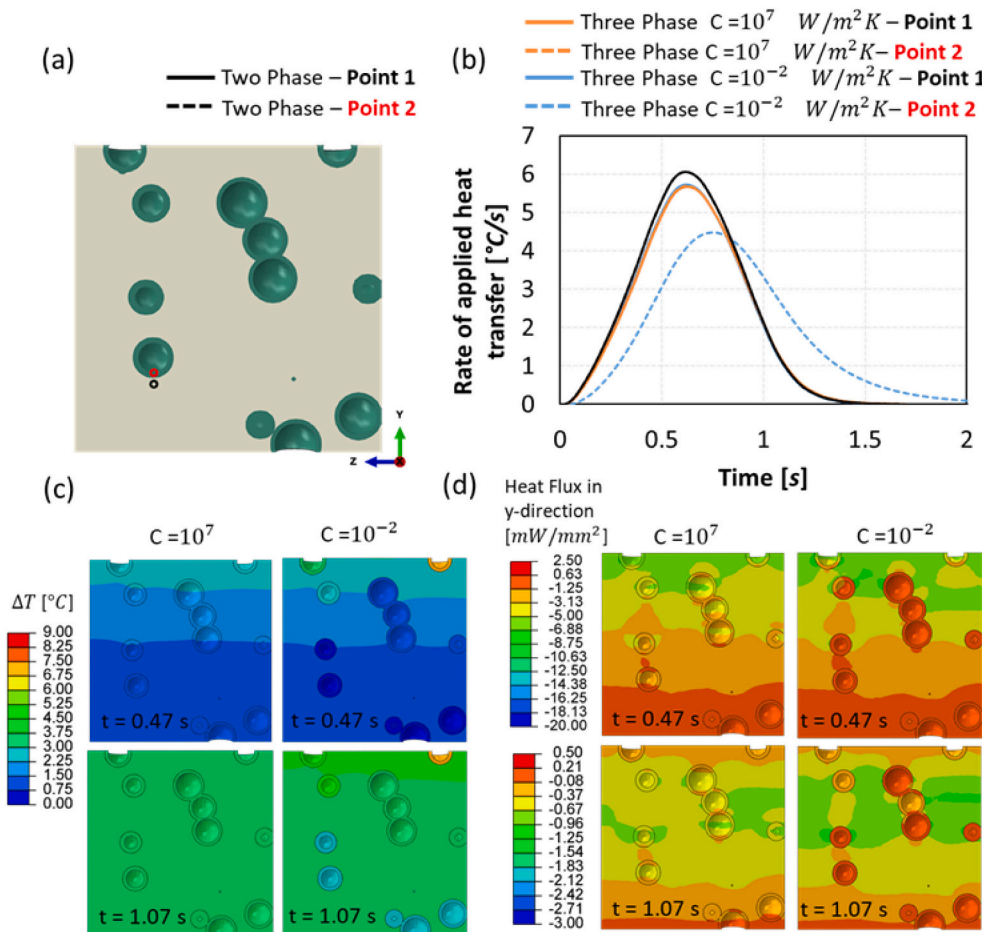

Fig. 12. Image (a) shows the middle cross-section of the RVE for the 15% micro-aerated chocolate considering the three-phase system assumption, image (b) shows the rate of applied heat transfer using the unsteady micro-FEM for two distinct locations (see black and red circle) for different micro-FEM approaches. The black and red point in image (a) refer to the location of the matrix close to the cocoa butter-chocolate matrix interface and the location inside the cocoa butter shell respectively. Images (c) shows the temperature difference distribution of the 15% micro-aerated chocolate for the case of relatively high and low interfacial thermal resistance and two distinct time steps. Image (d) shows the heat flux contour plots in the y-direction of the middle section of the RVE for two time steps assuming the chocolate as a three-phase system without and with interfacial thermal. The two-time steps in images (c) and (d) correspond to times before the peak of the heat pulse and after the removal of the heat.

the true properties of cocoa butter at the interface might differ from the ones computed using DSC instruments (see Table 1) because of the cocoa butter at the pore interface. Therefore, the higher melting point crystals might exhibit different thermal properties, which in turn, could affect the thermal response of chocolate, as already shown by the results of this study ("*two-phase*" vs "*three-phase*" models).

The presented computational model can accurately estimate the dependence of thermal properties, such as thermal conductivity and specific heat capacity, on porosity and, at the same time, predict the unsteady heat transfer phenomena under deferent loading scenarios. These scenarios are relevant to chocolate oral processing (heating and melting) but also to chocolate manufacturing process, such as cooling. The maximum 11% difference in the heat transfer response in chocolate with 15% micro-aeration between the two-phase and three-phase with interfacial resistance assumption, see Fig. 8, is believed to be capable to create differences in the oral perception when the chocolate is consumed. The ability of the micro-aerated chocolate to store higher amounts of thermal energy during heating compared to its reference counterpart could be responsible for a delayed melting process inside the mouth. This, in turn, could increase the flavour intensity and create a long-lasting perception of flavour during oral processing. Correlation between flavour attributes and chocolate's melting has been discussed in the literature in the past (Haedelt et al., 2007). This delayed melting process of the micro-aerated chocolate could affect the sweetness perception too. Sweetness is perceived when sugar crystals inside the chocolate are dissolved in the presence of saliva and trigger the taste buds in the oral cavity. A delaying melting of chocolate could, therefore, influence the number of sugar crystals exposed in the oral cavity, and by extension, slowing the dissolution of saliva, leaving an enhanced sweetness perception.

The difference in the heat transfer response between micro-aerated and non-aerated chocolate might be even more significant during the chocolate's manufacturing process. A delayed melting process in the case of the micro-aerated chocolate due to the reasons discussed in this work could result to an increased residence time of chocolates in cooling tunnels during the cooling process of the material.

Finally, it is important to highlight the versatility of the presented multiscale model, which can be applied to any composite or porous structure, food or otherwise, if the thermal properties of the material's constituents are well defined.

4. Conclusions

A multiscale Finite Element Model has been developed considering microstructural changes of chocolate due to micro-aeration. The multiscale computational model has successfully simulated the porous chocolate as either a two-phase (chocolate-pores) or a three-phase material (chocolate-cocoa butter shell-gas pores). For the latter case, the possibility of an additional thermal resistance mechanism in the form of interfacial resistance between the chocolate and cocoa butter interface was investigated. The results showed that the model predicts accurately the dependence of thermal properties, such as thermal conductivity and specific heat capacity, on porosity. On the other hand, the latent heat of chocolate was assumed to be independent of porosity. At the same time, more accurate predictions are obtained when the micro-porous chocolate is simulated as a three-phase system in comparison to the experimental data obtained from the heat transfer test rig. The results with the three-phase system approach that included the interfacial resistance of the chocolate-cocoa butter interface produced results of even higher accuracy. However, the cause of this thermal response phenomenon requires further investigation. The computational model might prove a useful design tool for the industry to estimate the melting behaviour of chocolate during food oral processing or/and simulate cooling during the manufacturing process.

References

Afoakwa, E. O., Paterson, A., Fowler, M., & Vieira, J. (2009). Microstructure and mechanical properties related to particle size distribution and composition in dark chocolate. *International Journal of Food Science and Technology, 44*(1), 111–119. https://doi.org/10.1111/j.1365-2621.2007.01677.x

Bikos, D. (2022). *Effect of micro-aeration on mechanical and thermal properties of chocolate and correlation to oral processing.* PhD, Imperial College London, London.

Bikos, D., et al. (2021a). Effect of structure on the mechanical and physical properties of chocolate considering time scale phenomena occurring during oral processing. *Food Structure, 31*, 100244. https://doi.org/10.1016/j.foostr.2021.100244

Bikos, D., et al. (2021b). Effect of micro-aeration on the mechanical behaviour of chocolates and implications for oral processing. *Food & Function, 12*, 4864–4886. https://doi.org/10.1039/D1FO00045D

Bikos, D., et al. (2022). Experimental and numerical evaluation of the effect of micro-aeration on the thermal properties of chocolate. *Food & Function, 13*(9), 4993–5010.

Binks, B. P., & Marinopoulos, I. (May 2017). Ultra-stable self-foaming oils. *Food Research International, 95*, 28–37. https://doi.org/10.1016/j.foodres.2017.02.020

Campbell, G. M., & Mougeot, E. (1999). Creation and characterisation of aerated food products. *Trends in Food Science and Technology, 10*(9), 283–296. https://doi.org/10.1016/S0924-2244(00)00008-X

Cao, C., Yu, A., & Qin, Q.-H. (2012). Evaluation of effective thermal conductivity of fiber-reinforced composites. *International Journal of Architecture, Engineering and Construction, 1*(1), 14–29. https://doi.org/10.7492/ijaec.2012.002

Carson, J. K., Lovatt, S. J., Tanner, D. J., & Cleland, A. C. (2006). Predicting the effective thermal conductivity of unfrozen, porous foods. *Journal of Food Engineering, 75*(3), 297–307. https://doi.org/10.1016/j.jfoodeng.2005.04.021

Carson, J. K., Wang, J., North, M. F., & Cleland, D. J. (Apr. 2016). Effective thermal conductivity prediction of foods using composition and temperature data. *Journal of Food Engineering, 175*, 65–73. https://doi.org/10.1016/j.jfoodeng.2015.12.006

Cernuschi, F., Ahmaniemi, S., Vuoristo, P., & Mäntylä, T. (2004). Modelling of thermal conductivity of porous materials: Application to thick thermal barrier coatings. *Journal of the European Ceramic Society, 24*(9), 2657–2667. https://doi.org/10.1016/j.jeurceramsoc.2003.09.012

Chen, Y. W., & Mackley, M. R. (2006). Flexible chocolate. *Soft Matter, 2*(4), 304–309. https://doi.org/10.1039/b518021j

Debaste, F., Kegelaers, Y., Liégeois, S., Ben Amor, H., & Halloin, V. (2008). Contribution to the modelling of chocolate tempering process. *Journal of Food Engineering, 88*(4), 568–575. https://doi.org/10.1016/j.jfoodeng.2008.03.019

Do, T. A. L., Hargreaves, J. M., Wolf, B., Hort, J., & Mitchell, J. R. (2007). Impact of particle size distribution on rheological and textural properties of chocolate models with reduced fat content. *Journal of Food Science, 72*(9), 541–552. https://doi.org/10.1111/j.1750-3841.2007.00572.x

Glicerina, V., Balestra, F., Dalla Rosa, M., & Romani, S. (2016). Microstructural and rheological characteristics of dark, milk and white chocolate: A comparative study. *Journal of Food Engineering, 169*, 165–171. https://doi.org/10.1016/j.jfoodeng.2015.08.011

Haedelt, J., Beckett, S. T., & Niranjan, K. (2007). Bubble-included chocolate: Relating structure with sensory response. *Journal of Food Science, 72*(3), 138–142. https://doi.org/10.1111/j.1750-3841.2007.00313.x

Hamdami, N., Monteau, J.-Y., & le Bail, A. (Nov. 2003). Effective thermal conductivity of a high porosity model food at above and sub-freezing temperatures. *International Journal of Refrigeration, 26*(7), 809–816. https://doi.org/10.1016/S0140-7007(03)00051-3

Huang, J. H. (1971). Effective thermal conductivity of porous rocks. *Journal of Geophysical Research, 76*(26), 6420–6427. https://doi.org/10.1029/JB076i026p06420

Jackson, G. V., & Leach, A. G. (1993). Thermal conductivity of foams. II: The thermal conductivity of a layer mineralfoam. *Journal of Physics D: Applied Physics, 26*(5), 740–745. https://doi.org/10.1088/0022-3727/26/5/004

Lee, S., Lee, J., Ryu, B., & Ryu, S. (Dec. 2018). A micromechanics-based analytical solution for the effective thermal conductivity of composites with orthotropic matrices and interfacial thermal resistance. *Scientific Reports, 8*(1). https://doi.org/10.1038/s41598-018-25379-8

Maleky, F., & Marangoni, A. (2011). Thermal and mechanical properties of cocoa butter crystallized under an external laminar shear field. *Crystal Growth & Design, 11*(6), 2429–2437. https://doi.org/10.1021/cg200202u

Marcos-Gómez, D., Ching-Lloyd, J., Elizalde, M. R., Clegg, W. J., & Molina-Aldareguia, J. M. (2010). Predicting the thermal conductivity of composite materials with imperfect interfaces. *Composites Science and Technology, 70*(16), 2276–2283. https://doi.org/10.1016/j.compscitech.2010.05.027

Minor, M., Vingerhoeds, M. H., Zoet, F. D., de Wijk, R., & van Aken, G. A. (2009). Preparation and sensory perception of fat-free foams - effect of matrix properties and level of aeration. *International Journal of Food Science and Technology, 44*(4), 735–747. https://doi.org/10.1111/j.1365-2621.2008.01887.x

Mishima, S., Suzuki, A., Sato, K., & Ueno, S. (Nov. 2016). Formation and microstructures of whipped oils composed of vegetable oils and high-melting fat crystals. *JAOCS, Journal of the American Oil Chemists' Society, 93*(11), 1453–1466. https://doi.org/10.1007/s11746-016-2888-4

Nan, C. W., Birringer, R., Clarke, D. R., & Gleiter, H. (May 1997). Effective thermal conductivity of particulate composites with interfacial thermal resistance. *Journal of Applied Physics, 81*(10), 6692–6699. https://doi.org/10.1063/1.365209

le Quang, H., He, Q. C., & Bonnet, G. (Sep. 2011). Eshelby's tensor fields and effective conductivity of composites made of anisotropic phases with Kapitza's interface thermal resistance. *Philosophical Magazine, 91*(25), 3358–3392. https://doi.org/10.1080/14786435.2011.580286

Reinke, S. K., et al. (2016). Synchrotron X-ray microtomography reveals interior microstructure of multicomponent food materials such as chocolate. *Journal of Food Engineering, 174*, 37–46. https://doi.org/10.1016/j.jfoodeng.2015.11.012

le Reverend, B. J. D., Fryer, P. J., & Bakalis, S. (2008). Modelling crystallization and melting kinetics of cocoa butter in chocolate and application to confectionery manufacturing. *Soft Matter, 4*(6), 1147–1150. https://doi.org/10.1039/b800106e

Rousseau, D., & Smith, P. (2008). Microstructure of fat bloom development in plain and filled chocolate confections. *Soft Matter, 4*(8), 1706–1712. https://doi.org/10.1039/b718066g

Rovers, T. A. M., Sala, G., van der Linden, E., & Meinders, M. B. J. (2016). Potential of microbubbles as fat replaces: Effect on rheological, tribological and sensorial properties of model food systems. *Texture Studies, 47*(3), 220–230. https://doi.org/10.1111/jtxs.12175

Samaras, G. (2021). *Oral processing of micro-aerated chocolates: A computational mechanics, rheological and tribological study*. PhD, Imperial College London, London.

Samaras, G., et al. (2020). Measurement of molten chocolate friction under simulated tongue-palate kinematics: Effect of cocoa solids content and aeration. *Current Research in Food Science, 3*, 304–313. https://doi.org/10.1016/j.crfs.2020.10.002

Shah, K. K., Tong, C. H., & Lund, D. B. (Sep. 2000). Methodology to obtain true thermal conductivity of low porosity food powders. *Journal of Food Science, 65*(6), 962–966. https://doi.org/10.1111/j.1365-2621.2000.tb09400.x

Simulia. (2017). *Abaqus 6.11 theory manual*. Providence, RI, USA: DS SIMULIA Corp.

Singh, I. V., Tanaka, M., & Endo, M. (2007). Effect of interface on the thermal conductivity of carbon nanotube composites. *International Journal of Thermal Sciences, 46*(9), 842–847. https://doi.org/10.1016/j.ijthermalsci.2006.11.003

Skamniotis, C. G., Edwards, C. H., Bakalis, S., Frost, G., & Charalambides, M. N. (2020). Eulerian-Lagrangian finite element modelling of food flow-fracture in the stomach to engineer digestion. *Innovative Food Science and Emerging Technologies, 66*. https://doi.org/10.1016/j.ifset.2020.102510

Skamniotis, C. G., Elliott, M., & Charalambides, M. N. (2017). On modeling the large strain fracture behaviour of soft viscous foods. *Physics of Fluids, 29*(12). https://doi.org/10.1063/1.4993754

Smith, D. S., et al. (Sep. 2013). Thermal conductivity of porous materials. *Journal of Materials Research, 28*(17), 2260–2272. https://doi.org/10.1557/jmr.2013.179

Zhang, H., Fang, W. Z., Li, Y. M., & Tao, W. Q. (2017). Experimental study of the thermal conductivity of polyurethane foams. *Applied Thermal Engineering, 115*, 528–538. https://doi.org/10.1016/j.applthermaleng.2016.12.057